High-Resolution Microwave Photonic Sparse Imaging Radar

Cong Ma, Xiangchuan Wang, Zeyong Ding, Zhijian Zhang, and Shilong Pan, *Fellow, IEEE*

***Abstract*— The escalating demand for high-resolution microwave imaging in modern applications has driven radar toward wider bandwidths and higher frequencies. Microwave photonics emerges as an innovative solution for radar development by surmounting the frequency and bandwidth limitations of conventional electronics. However, using a continuous wideband spectrum for a high-resolution microwave radar is hindered by the increasingly congested spectra. Herein, we propose a novel high-resolution microwave photonic sparse imaging radar that employs sparse spectra and sparse apertures to reconcile the conflict between high resolution and continuous wide bandwidth. A wideband random sparse stepped-frequency chirp signal is generated based on recirculating microwave photonic frequency conversion (MWP-FC) and rapidly preprocessed by photonic dechirping. In addition, a sparse signal recovery method, the convolutionally enhanced smoothed ℓ_0 algorithm, is proposed to process the undersampled dechirped signals resulting from sparse spectra and sparse apertures. This method enhances the local structural features of radar images and achieves robust high-resolution sparse imaging. A practical implementation of radar with a frequency range exceeding 16 GHz while effectively occupying only a 4-GHz spectrum is demonstrated, realizing a range resolution of 8.3 mm. We also demonstrate the feasibility and superiority of high-resolution sparse range imaging and sparse inverse synthetic aperture radar (SAR) imaging, thereby making a substantial contribution to the advancement of microwave imaging and offering promising prospects for applications such as intelligent transport, safety monitoring, and topographic mapping.**

***Index Terms*— High resolution, microwave photonics, radar, sparse imaging.**

I. Introduction

MODERN applications, such as intelligent transport, safety monitoring, and topographic mapping, increasingly demand high-resolution microwave radar, which provides solid support for microwave imaging by capturing echoes with abundant target information. In contrast to optical imaging systems, microwave imaging radars enable all-day, all-weather, and long-range working, benefiting from microwave signals with penetrating capabilities [1]. In microwave imaging radars, the range resolution is inversely proportional to the bandwidth of radar signals, while the cross-range resolution or azimuth resolution is inversely proportional to an antenna aperture [2]. Therefore, wide bandwidth microwave signals and large apertures are required to achieve high-resolution radar imaging.

However, bandwidth bottlenecks in electronics limit the capability of conventional microwave radars to generate, transmit, and process wideband signals, seriously limiting the range resolution. In recent years, researchers have shown an increased interest in microwave photonics and endeavored to apply it to radar due to its unparalleled advantages over electronics in wideband signal generation and processing [3], [4], [5], [6], [7], [8]. Optical frequency doubling and dechirping are prevalent in microwave photonic radars, facilitating high-resolution fast or even real-time imaging [9], [10], [11], [12], [13], [14], [15]. In these systems, the continuous expansion of radar signal bandwidth necessitates an increment in the frequency doubling number, which may induce additional harmonics. A high-resolution radar can be constructed utilizing an optical digital-to-analog converter (DAC) [16]. Nevertheless, the bandwidth of the optical DAC is ultimately constrained to the digital drive signal rate of an electrical signal generator (ESG). A microwave photonic radar can also be realized based on optical injection semiconductor lasers, without requiring a radio frequency (RF) source [17], [18]. However, the signal-to-noise ratio (SNR) obtained from this scheme is significantly influenced by the laser linewidth, as the secondary laser operates in the period-one dynamic and is not locked to the main laser. Although signals generated by a Fourier domain mode locking optoelectronic oscillator (FDML-OEO) can attain a relatively high SNR [19], the realization of wideband signal oscillation is challenging due to phase mismatch limitations. Ultrawide bandwidth radar systems can also be constructed based on optical recirculating frequency shifting (OFSL), significantly reducing the dependence on wideband ESGs [20], [21], [22]. However, the employment of optical heterodyne in such systems leads to the conversion of optical phase noise into microwave signals, thereby degrading the radar signal performance.

Moreover, most of the above studies have neglected that the electromagnetic environment is becoming increasingly complex, and frequency spectrum resources are becoming increasingly scarce [23]. It is now more difficult to allocate sufficient wideband spectrum for a high-resolution radar. A promising way to address these issues is to further leverage sparse radar signals to avoid interference. Based on microwave photonic technologies, it is expected to generate

Received 21 October 2024; revised 10 January 2025; accepted 28 January 2025. Date of publication 14 February 2025; date of current version 15 August 2025. This work was supported in part by the National Natural Science Foundation of China under Grant 62271249 and Grant 62075095, and in part by the Fundamental Research Funds for the Central Universities. *(Corresponding authors: Xiangchuan Wang; Shilong Pan.)*

The authors are with the National Key Laboratory of Microwave Photonics, Nanjing University of Aeronautics and Astronautics, Nanjing 210016, China (e-mail: wangxch@nuaa.edu.cn; pans@nuaa.edu.cn).

Digital Object Identifier 10.1109/TMTT.2025.3538545

sparse radar signals with a large frequency coverage, thus fully utilizing the available spectrum resources over a wide range for target detection. This is an arduous task to achieve with conventional electronics. For instance, the bandwidth of direct digital synthesizers (DDSs) typically used in radar is merely a few gigahertz [24], [25]. There are many sparse signal generation methods based on microwave photonics, such as optically injected semiconductor lasers [26], FDML-OEO [27], and OFSL [28], [29], but they have the same limitations as previously described. In [29], we demonstrate a high-resolution radar based on the sparse stepped-frequency chirp (SSFC) signals generated by an OFSL, in which the deterioration of the generated signal due to laser phase noise is ignored. Thus, an expensive narrow linewidth laser is required in the OFSL-based system. We previously proposed a signal generation method based on recirculating microwave photonic frequency conversion (MWP-FC) to effectively eliminate the influence of laser phase noise [30], but the spectral distribution of the generated signals is uniform, which is difficult to satisfy the demand for sparse radar for random spectrum. Furthermore, a large virtual aperture is usually synthesized based on the relative motion between the target and the radar as well as observing the target with a long coherent processing interval (CPI) to achieve high azimuth resolution because it is challenging to build an actual large aperture antenna in practical scenarios [31]. Even if a sparse signal is employed, it is difficult to ensure that the radar remains free from interference within a complex electromagnetic environment over a long CPI. Consequently, certain potential environmental noise or interference may lead to the absence of some bursts, resulting in incomplete sampling in the azimuth direction, i.e., sparse aperture [32]. However, this crucial aspect is neglected in [29].

In signal processing, the conventional range–Doppler (RD) imaging algorithm fails to work due to the presence of sparse spectra and possible sparse apertures. Fortunately, the target image can be further recovered using the sparsity of the radar image because microwave images usually consist of strongly scattering points that fill up a small number of pixels in the image. There has been extensive research on sparsity-driven imaging methods based on sparse signal recovery for traditional narrowband microwave radar [33], [34], [35]. These efforts have improved radar imaging resolution and reduced data acquisition time and volume. Currently, most microwave photonic systems still follow these traditional algorithms, without providing targeted improvements for microwave photonic radar's high-resolution features. The commonly used approaches in microwave image reconstruction are 1-D sparse signal recovery algorithms, such as OMP [36], fast iterative shrinkage threshold algorithm (FISTA) [37], and smoothed ℓ_0 (SL0) [38]. It is possible to reconstruct the range image or azimuth image separately using a 1-D algorithm [29], [39], but this inevitably corrupts the association between different azimuths or ranges in 2-D imaging. The undersampled 2-D signal matrix can also be converted to a 1-D vector in the 2-D imaging, which is then processed with the 1-D algorithm [40]. However, the required observation matrix is very large, leading to huge memory and computational costs. Recently, some 2-D signal recovery algorithms, such as 2-D-OMP [41], 2-D-FISTA [42], and 2-D-SL0 [43], have been developed to ameliorate these problems. Among them, the 2-D-SL0 algorithm can obtain sparser solutions based on less data, but it faces the drawbacks of sensitivity to noise and low robustness. Further exploiting and utilizing a priori information from radar imaging is expected to improve the imaging performance. For example, scatterers on a target may occupy multiple adjacent resolution cells rather than exist in isolation, which is particularly common in high-resolution microwave photonic radar imaging. However, most algorithms regularly neglect this structure in radar imaging, so the reconstruction results are usually unsatisfactory. Although the group SL0 (GSL0) algorithm enhances the structural features by grouping the sparse signal, it is still difficult to obtain satisfactory results because the groups are relatively independent [44].

This article proposes and demonstrates a microwave photonic radar for high-resolution sparse imaging. In contrast to previous works [29], [30], we generate random SSFC signals based on recirculating MWP-FC, thereby further enhancing the radar's flexibility and practicality. The proposed system also accounts for the sparse aperture potentially induced by interferences, which is neglected in [29]. In addition, we present a sparse radar imaging method based on a convolutionally enhanced SL0 (CSL0) norm. This method exploits convolution to enhance the local structural features of the radar image, subsequently elevating the quality of image reconstruction. The CSL0 algorithm can be implemented for both 1-D range image reconstruction and 2-D microwave image reconstruction. In the process of 2-D microwave image reconstruction, the signal matrix is processed directly instead of vectorization, avoiding a huge observation matrix. Thus, the memory is reduced, while the processing speed is increased. In the experiment, we successfully realized high-resolution and highly robust ranging and imaging, validating the feasibility and superiority of the proposed method.

II. System Configuration and Imaging Model

A. System Configuration

Fig. 1 shows the schematic of the proposed microwave photonic radar. In the transmitter, random sparse stepped-frequency chirp (SSFC) signals are generated based on an MWP-FC loop, which is mainly composed of a laser diode (LD), a dual-parallel Mach–Zehnder modulator (DPMZM), a fiber spool, an optical amplifier (OA), an optical bandpass filter (OBPF), a photodetector (PD), a low noise amplifier (LNA), and a microwave 90° hybrid.

The MWP-FC loop has two RF inputs: a microwave-driving chirp signal (RF1) with a narrow bandwidth and a microwave reference signal (RF2) consisting of several subpulses with randomly fluctuating frequencies. The center frequency and chirp rate of the chirp signal are denoted as f_c and γ, respectively, and the frequency of the ith subpulse of the reference signal is f_{ri}. The two RF signals are fed into the DPMZM via the microwave 90° hybrid to modulate the optical carrier from the LD with a frequency of f_L. The DPMZM operates in a carrier-suppressed single-sideband (CS-SSB) mode [29]. It should be noted that the two RF signals are

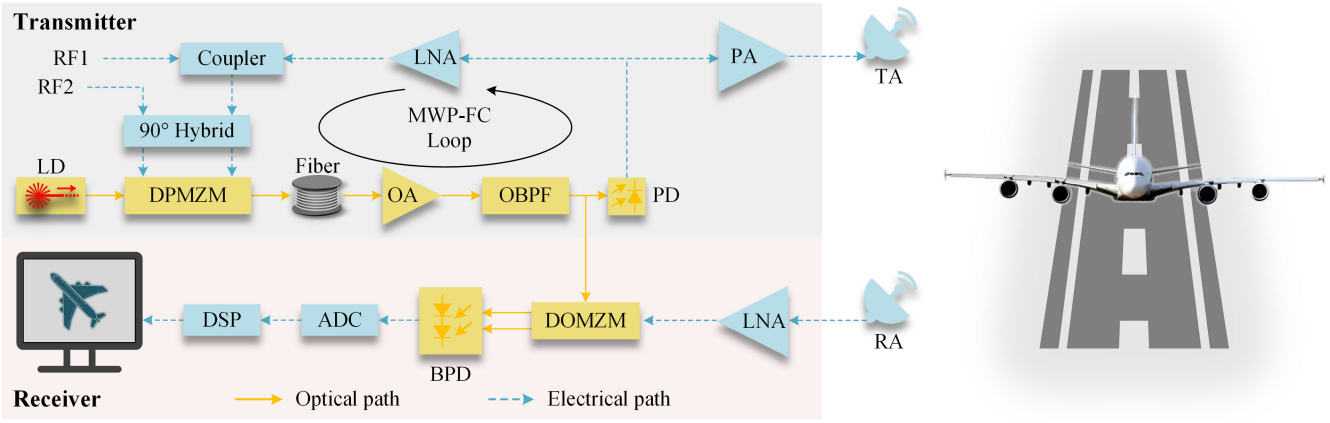

Fig. 1. Schematic of the proposed microwave photonic radar. MWP-FC: microwave photonic frequency conversion. LD: laser diode. DPMZM: dual-parallel Mach–Zehnder modulator. OA: optical amplifier. OBPF: optical bandpass filter. PD: photodetector. DOMZM: dual output Mach–Zehnder modulator. BPD: balanced PD. RF: radio frequency. LNA: low noise amplifier. PA: power amplifier. TA: transmit antenna. RA: receiver antenna. ADC: analog-to-digital converter. DSP: digital signal processor.

fed into two different input ports of the microwave 90° hybrid. As a result, the sidebands caused by the two RF signals are located on different sides of the optical carrier. The optical signal output by the DPMZM is amplified by an OA after propagating through a fiber spool. Subsequently, an OBPF is used to control the loop bandwidth as well as to filter out the amplified spontaneous emission (ASE) noise. The optical signal output from the OBPF is split into two paths. One path is sent to the receiver as an optical reference signal, while the other path is sent to a PD. In the PD, the two sidebands are beaten to produce a frequency-converted microwave signal. The phase noise caused by the optical carrier is the same for both sidebands and is canceled after optoelectric conversion [30]. The PD output signal is also divided into two portions. One portion is amplified by a power amplifier (PA) and radiated through a transmit antenna (TA). The other portion is amplified by an LNA and then fed back into the loop. The optical spectrum of the DPMZM output in the nth frequency conversion is shown in Fig. 2, where the dashed lines and shadow regions indicate the spectrum before the nth frequency conversion. At this stage, the microwave chirp signal at the DPMZM input is the $(n-1)$st output of the loop, and its center frequency is $f_c + f_{rn-1} + \cdots + f_{r1}$. The chirp signal induces the sidebands on the left side of the optical carrier, with a center frequency of $f_L - f_c - f_{rn-1} - \cdots - f_{r1}$. The input microwave reference signal with a frequency of f_{rn} induces the sidebands on the right side of the optical carrier, with a frequency of $f_L + f_{rn}$. After successive frequency conversion, a random SSFC signal is obtained and written as

$$s_{\mathrm{SSFC}}(t) \propto \sum_{n=1}^{N_{\max}} \mathrm{rect}\left(\frac{t-nT_L}{T_{\mathrm{pw}}}\right) \cdot \cos\left\{2\pi\left[\left(f_c + \sum_{i=1}^{n} f_{ri}\right)(t-nT_L) + \frac{1}{2}\gamma(t-nT_L)^2\right] + \phi_n\right\} \quad (1)$$

where $\mathrm{rect}(x) = \{1, |x| \le 0.5; 0, |x| > 0.5\}$, $N_{\max}$ is the maximum frequency conversion number determined by the loop bandwidth, T_L is the delay of the frequency conversion loop, T_{pw} is the pulsewidth of the driving pulse, and ϕ_n is the initial phase of the nth subpulse. Thanks to the constant frequency conversion, the bandwidth of the generated random SSFC signal is greatly augmented compared to the input microwave chirp signal. Moreover, the randomly stepped frequencies would enhance the anti-interception capability of a radar.

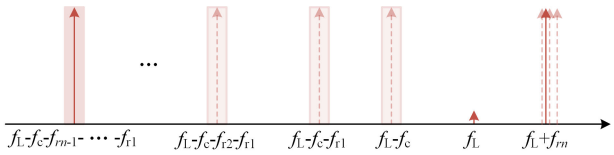

Fig. 2. Optical spectrum of the DPMZM output in the nth frequency conversion. The dashed lines and shadow regions indicate the spectrum before the nth frequency conversion.

The echo reflected by the target is collected by a receive antenna (RA) and sent to the receiver. Within the receiver, the amplified echo modulates the optical reference signal via a DOMZM, which is biased at the quadrature transmission point. The optical signal output from the DOMZM is then sent to a balanced PD (BPD) for dechirping. The distance R determines the time delay τ between the echo and transmitted radar signal through $\tau = 2R/c$, where c is the light speed. Consequently, the generated dechirped signal can be written as

$$s_{\mathrm{de}}(t) \propto \sum_{n=1}^{N_{\max}} \mathrm{rect}\left(\frac{t-nT_L-\tau}{T_{\mathrm{pw}}-\tau}\right) \cdot \cos\left\{2\pi\left[\gamma\tau(t-nT_L) + \left(f_c + \sum_{i=1}^{n} f_{ri}\right)\tau - \gamma\tau^2/2\right]\right\}. \quad (2)$$

The dechirped signal usually has a sufficiently low frequency $\Delta f = \gamma\tau$ compared to the wideband radar signal. Therefore, it can be sampled and processed by low-speed electronics with high precision.

A high-resolution range image can be obtained by bandwidth synthesis when the frequencies between subpulses of

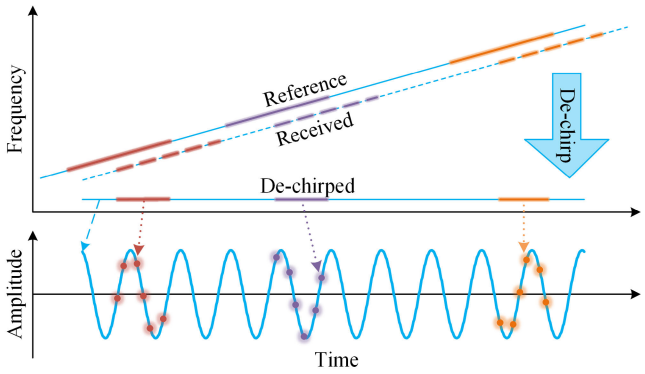

Fig. 3. Illustration of the undersampling process.

the SSFC signal are continuous [20]. However, allocating a large continuous spectrum to radar in most scenarios is difficult. In this work, we set the frequency of the SSFC signal to be sparse by making its subpulse bandwidth smaller than the stepped frequencies. In this way, the occupation of the spectrum resources can be effectively reduced. It should be noted that this leads to phase discontinuities between the subpulses of the dechirped signal, further leading to strong spurs in the image [29]. Therefore, a novel processing method is required, considering that bandwidth synthesis fails to process such subpulses.

B. Sparse Range Imaging Model

The range image can be obtained by applying the 1-D Fourier transform on the full signal. Consequently, we obtain the following expression in the vector form:

$$\boldsymbol{s} = \boldsymbol{F}_r^{-1}\boldsymbol{x} + \boldsymbol{\eta} \tag{3}$$

where $\boldsymbol{s} \in \mathbb{C}^{M\times 1}$ is the full dechirped signal, $\boldsymbol{F}_r^{-1} \in \mathbb{C}^{M\times M}$ represents an inverse discrete Fourier transform (IDFT) matrix, $\boldsymbol{x} \in \mathbb{C}^{M\times 1}$ means the range image, and η denotes the noise vector.

The dechirped signal of the random SSFC signal can be regarded as an undersampling of the full dechirped signal, as shown in Fig. 3, and can be represented as

$$\boldsymbol{y} = \boldsymbol{\Phi}_r\boldsymbol{s} + \boldsymbol{\eta} = \boldsymbol{\Phi}_r\boldsymbol{F}_r^{-1}\boldsymbol{x} + \boldsymbol{\eta} = \boldsymbol{A}\boldsymbol{x} + \boldsymbol{\eta} \tag{4}$$

where $\boldsymbol{y} \in \mathbb{C}^{m\times 1}$ is the undersampled signal, $\boldsymbol{\Phi}_r \in \mathrm{R}^{m\times M}$ denotes an undersampling matrix, and $\boldsymbol{A} \in \mathbb{C}^{m\times M}$ indicates $\boldsymbol{\Phi}_r\boldsymbol{F}_r^{-1}$ for convenience.

Because the radar range image is usually sparse, the reconstruction of $\boldsymbol{s}$ or $\boldsymbol{x}$ becomes an optimization model

$$(P_0):\ \min_{\boldsymbol{x}} ||\boldsymbol{x}||_0, \quad \text{s.t. } ||\boldsymbol{y} - \boldsymbol{A}\boldsymbol{x}||_2^2 \le \varepsilon \tag{5}$$

where $||\boldsymbol{x}||_0$ is the ℓ_0 norm of $\boldsymbol{x}$ and ε is an error threshold.

C. Sparse ISAR Imaging Model

A synthetic aperture radar (SAR) or inverse SAR (ISAR) model can be constructed when there is relative motion between the target and the radar. In this study, an ISAR is taken as an example to verify the performance of the proposed system. Here, we assume that the translation of the target is compensated and employ a turntable model for ISAR imaging [31]. Assuming a small rotation angle of the target, an ISAR image can be obtained by applying the 2-D Fourier transform on the full dechirped signal matrix along the distance and azimuth directions. Thus, we obtain the following expression in the matrix form:

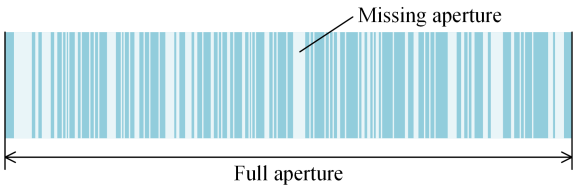

Fig. 4. Schematic of sparse aperture.

$$\boldsymbol{S} = \boldsymbol{F}_r^{-1}\boldsymbol{X}\boldsymbol{F}_a^{-1} + \boldsymbol{N} \tag{6}$$

where $\boldsymbol{S} \in \mathbb{C}^{M\times N}$ is the full dechirped signal matrix, $\boldsymbol{F}_r^{-1} \in \mathbb{C}^{M\times M}$ and $\boldsymbol{F}_a^{-1} \in \mathbb{C}^{N\times N}$ represent an IDFT matrix, $\boldsymbol{X} \in \mathbb{C}^{M\times 1}$ means the ISAR image, and $\boldsymbol{N}$denotes the noise matrix.

In this work, we consider the sparse aperture in addition to using random SSFC signals to reduce the amount of data while improving the radar's immunity to interference, as shown in Fig. 4. This process can be viewed as the undersampling of the dechirped signal. Thus, the obtained dechirped signals are represented as

$$\boldsymbol{Y} = \boldsymbol{\Phi}_r\boldsymbol{S}\boldsymbol{\Phi}_a + \boldsymbol{N} = \boldsymbol{\Phi}_r\boldsymbol{F}_r^{-1}\boldsymbol{X}\boldsymbol{\Phi}_a\boldsymbol{F}_a^{-1} + \boldsymbol{N} = \boldsymbol{A}\boldsymbol{X}\boldsymbol{B} + \boldsymbol{N} \tag{7}$$

where $\boldsymbol{Y} \in \mathbb{C}^{m\times n}$ is the undersampled signal matrix; $\boldsymbol{\Phi}_r \in \mathrm{R}^{m\times M}$ and $\boldsymbol{\Phi}_a \in \mathrm{R}^{N\times n}$ denote an undersampling matrix; and $\boldsymbol{A} \in \mathbb{C}^{m\times M}$ and $\boldsymbol{B} \in \mathbb{C}^{N\times n}$ indicate $\boldsymbol{\Phi}_r\boldsymbol{F}_r^{-1}$ and $\boldsymbol{\Phi}_a\boldsymbol{F}_a^{-1}$ for convenience, respectively.

A common approach for solving $\boldsymbol{X}$ is vectorizing $\boldsymbol{Y}$ and $\boldsymbol{X}$ into a 1-D vector [40]. Thus, an observation matrix with a size of $mn \times MN$ is required, resulting in excessive memory usage and slow processing speed. For example, a 2-D signal $\boldsymbol{X} \in \mathbb{C}^{100\times 50}$ is compressed by $\boldsymbol{A} \in \mathbb{C}^{40\times 100}$ and $\boldsymbol{B} \in \mathbb{C}^{50\times 30}$ to produce $\boldsymbol{Y} \in \mathbb{C}^{40\times 30}$. If a 1-D model is used through vectorization, an observation matrix $\boldsymbol{\Phi} \in \mathbb{C}^{1200\times 5000}$ will be necessary. Evidently, the matrix $\boldsymbol{\Phi}$ will consume more computational resources and reduce the computational speed compared to matrices $\boldsymbol{A}$ and $\boldsymbol{B}$. Here, we use a 2-D model directly, i.e., formulating the reconstruction of $\boldsymbol{X}$ as an optimization problem

$$(P_1):\ \min_{\boldsymbol{X}} ||\boldsymbol{X}||_0, \quad \text{s.t. } ||\boldsymbol{Y} - \boldsymbol{A}\boldsymbol{X}\boldsymbol{B}||_2^2 \le \varepsilon \tag{8}$$

where $||\boldsymbol{X}||_0$ is the ℓ_0 norm of $\boldsymbol{X}$ and ε is an error threshold.

III. Sparse Imaging Methods

A. Optimization Model Based on CSL0 Norm

The ℓ_0 norm function, which can accurately characterize signal sparsity, is highly discontinuous, and its minimization is nondeterministic polynomial (NP)-hard. Some approximate functions are usually adopted to tackle this issue. The most

commonly encountered is the ℓ_1 norm, a convex function. It facilitates the solution in optimization. We can also design or choose other suitable smooth functions to approximate the ℓ_0 norm, such as the Gaussian function [38]

$$f_\sigma(x_{ij}) = \exp\left(-\frac{x_{ij}^2}{2\sigma^2}\right) \tag{9}$$

where x_{ij} is the element in the matrix $\boldsymbol{X}$ and σ is a parameter.

Note the above function has a property that

$$\lim_{\sigma\to 0} f_\sigma(x_{ij}) = \begin{cases} 1, & x_{ij} = 0 \\ 0, & x_{ij} \neq 0. \end{cases} \tag{10}$$

This method of using a smooth function instead of the ℓ_0 norm is called the smoothed ℓ_0 (SL0) norm, which provides better results than the ℓ_1 norm-based method. The above function takes isolated elements in the image as independent variables, ignoring the relationship between them. However, in high-resolution microwave photonic radar, the target typically occupies multiple adjacent high-resolution resolution cells, i.e., there are some nonzero groups. In other words, it may have group sparsity. Here, we propose a convolution-enhanced smoothing ℓ_0 (CSL0) norm.

We define

$$\boldsymbol{W} = |\boldsymbol{X}|^2 * \boldsymbol{Ker} \tag{11}$$

where $|\boldsymbol{X}|^2$ represents the square of the modulus of the elements in $\boldsymbol{X}$, the symbol "$*$" denotes a convolutional computation, and $\boldsymbol{Ker}$ is the convolutional kernel.

By substituting the elements w_{ij} in $\boldsymbol{W}$ into (9), we have

$$f_\sigma(w_{ij}) = \exp\left(-\frac{w_{ij}}{2\sigma^2}\right). \tag{12}$$

Next, we define

$$\lim_{\sigma\to 0} F_\sigma(\boldsymbol{X}) = \sum_{i=1}^{M}\sum_{j=1}^{N} f_\sigma(w_{ij}) = MN - ||\boldsymbol{X}||_0 \tag{13}$$

where M and N are the number of elements in rows and columns of $\boldsymbol{X}$, respectively.

Therefore, the minimization problem P_1 is reformulated as

$$(P_2):\ \max_{\boldsymbol{X}} \lim_{\sigma\to 0} F_\sigma(\boldsymbol{W}), \quad \text{s.t. } ||\boldsymbol{Y} - \boldsymbol{AXB}||_2^2 \le \varepsilon. \tag{14}$$

B. Model Solving

The parameter σ determines the approximation of P_1 to P_2. The smaller σ is, the more approximate it is. However, $F_\sigma(\boldsymbol{W})$ contains multiple local maxima when σ is small. In this case, it is difficult to find a globally optimal solution. In contrast, the global optimal solution is easily solved without local maxima for sufficiently large σ. Similar to the classic SL0 algorithm, two layers of loops are designed to avoid getting trapped in local maxima. In the outside loop, σ is decreased, while fixed in the internal loop. The steepest ascent approach is used in the internal loop to maximize $F_\sigma(\boldsymbol{W})$.

In the following, we give a brief description of the algorithm. The gradient of $F_\sigma(\boldsymbol{W})$ with respect to $\boldsymbol{X}$ is expressed as

$$\nabla_{\boldsymbol{X}} F_\sigma(\boldsymbol{W}) = -\frac{1}{\sigma^2}\boldsymbol{X} \odot \exp\left(-\frac{\boldsymbol{W}}{2\sigma^2}\right) \tag{15}$$

Algorithm 1: CSL0

Input: $\boldsymbol{Y}$, $\boldsymbol{Ker}$, $\boldsymbol{A}$, $\boldsymbol{A}^\dagger$, $\boldsymbol{B}$, $\boldsymbol{B}^\dagger$, $\sigma_{\min}$, μ, L, $0<a<1$
Initialization: $\boldsymbol{X}=\boldsymbol{A}^\dagger\boldsymbol{Y}\boldsymbol{B}^\dagger$, $\sigma=2\max(|\boldsymbol{X}|)$
while $\sigma>\sigma_{\min}$
  for $i=1,\ldots,L$
    Compute: $\boldsymbol{W} = |\boldsymbol{X}|^2 * \boldsymbol{Ker}$
    Update: $\boldsymbol{X} \leftarrow \boldsymbol{X} - \mu\boldsymbol{X} \odot \exp(-\frac{\boldsymbol{W}}{2\sigma^2})$
    Project: $\boldsymbol{X} \leftarrow \boldsymbol{X} - \boldsymbol{A}^\dagger(\boldsymbol{AXB} - \boldsymbol{X})\boldsymbol{B}^\dagger$
  end for
  $\sigma \leftarrow a\times\sigma$
end while
Output: $\boldsymbol{X}$

Fig. 5. CSL0 algorithm flow.

where the symbol "$\odot$" denotes the matrix element multiplication. Next, update $\boldsymbol{X}$ by a gradient ascent step

$$\boldsymbol{X} \leftarrow \boldsymbol{X} + \mu_\sigma \nabla_{\boldsymbol{X}} F_\sigma(\boldsymbol{W}). \tag{16}$$

In the steepest ascent approach, $\mu_\sigma = \mu\sigma^2$, so we have

$$\boldsymbol{X} \leftarrow \boldsymbol{X} - \mu\boldsymbol{X} \odot \exp\left(-\frac{\boldsymbol{W}}{2\sigma^2}\right). \tag{17}$$

Then, project $\boldsymbol{X}$ back to the feasible set

$$\boldsymbol{X} \leftarrow \boldsymbol{X} - \boldsymbol{A}^\dagger(\boldsymbol{AXB} - \boldsymbol{X})\boldsymbol{B}^\dagger \tag{18}$$

where the symbol "$\dagger$" denotes pseudoinverse.

Repeat the calculations for L times according to (16)–(18) and then break out of the internal loop. Afterward, decrease σ and start a new outer loop until the solution converges. For convenience, we name the proposed algorithm as the CSL0 algorithm and summarize it in Algorithm 1, as shown in Fig. 5.

Algorithm 1 can be employed to solve the 2-D model directly without vectorizing the matrix as in conventional methods, avoiding the use of a large observation matrix and reducing memory consumption. When $N = 1$ or $M = 1$, the model becomes a 1-D vector model. Thus, the 1-D model can be regarded as a particular case of the 2-D model. For the 1-D model, matrix $\boldsymbol{A}$ or $\boldsymbol{B}$ can be omitted in the optimization calculation process. Hence, Algorithm 1 can also be used for range imaging reconstruction.

It should be noted that a large rotation angle of the target can achieve high azimuth resolution in an ISAR, but it may lead to range cell migration and image defocus. This contradiction is prevalent in wideband microwave photonic ISAR imaging. In this work, we mitigate the mentioned problems using the keystone transform and the entropy-based autofocus algorithm [31].

C. Simulation and Analysis

This section analyzes the proposed CSL0 algorithm through several simulations to verify its feasibility and superiority in radar imaging reconstruction.

First, the performance of the CSL0 algorithm to reconstruct the range image is simulated and analyzed. The key parameters

TABLE I
PARAMETERS FOR RANGE IMAGE RECONSTRUCTION SIMULATION

Bandwidth of subpulse	0.5 GHz
Pulse width of subpulse	4 μs
Number of subpulse	8
Number of scatter	5
Sampling rate	10 MHz

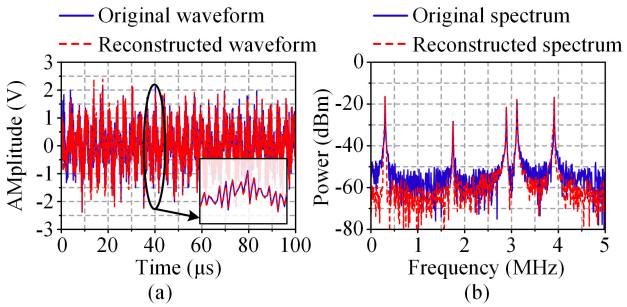

Fig. 6. Comparison of reconstructed and original (a) waveforms and (b) spectra.

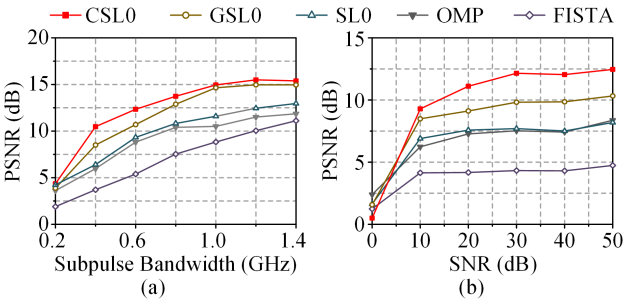

Fig. 7. PSNRs at different (a) subpulse bandwidths and (b) SNRs.

used in the simulation are shown in Table I. The stepped frequencies between the subpulses are randomly varying and the subpulses are randomly distributed over a frequency range of about 17.71 GHz. During the signal processing, we set $\boldsymbol{Ker} = [0.3\ 0.7\ 1\ 0.7\ 0.3]$, $a = 0.9$, and $\mu = 0.8$. In addition, a chirp signal with a bandwidth of 17.71 GHz is set up to evaluate the reconstruction performance of the sparse signal processing algorithm. The original waveform and spectrum of the dechirped signal obtained based on the chirp signal are shown as the blue curves in Fig. 6(a) and (b), respectively.

The reconstructed waveform and spectrum using the proposed CSL0 algorithm are shown as red dashed lines in Fig. 6(a) and (b), respectively. The red dashed line and the blue curve in both the reconstructed waveform and the reconstructed spectrum are highly coincident. This result proves the effectiveness of the proposed CSL0 algorithm. The reconstruction performance is further investigated for different subpulse bandwidths of the SSFC signal and SNRs of the dechirped signal. The subpulse bandwidth is equal to the bandwidth of the input microwave chirp signal of the MWP-FC loop, while the SNR represents the ratio of the dechirped signal power to all the noise power. We use the peak SNR (PSNR) for quantification in the reconstruction performance evaluation.

0.3	0.3	0.3	0.3	0.3
0.3	0.7	0.7	0.7	0.3
0.3	0.7	1	0.7	0.3
0.3	0.7	0.7	0.7	0.3
0.3	0.3	0.3	0.3	0.3

Fig. 8. Values of the 2-D convolution kernel Ker.

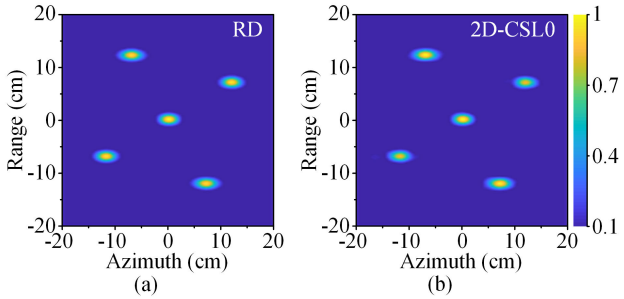

Fig. 9. ISAR images based on different methods. (a) RD. (b) 2-D-CSL0.

The results are shown in Fig. 7, which also shows the results of several popular methods, such as GSL0, SL0, OMP, and FISTA. As can be seen, the PSNR shows an increasing trend as the subpulse bandwidth and the SNR increase, and the reconstruction result of the CSL0 algorithm is the best among the considered solutions.

Then, the performance of the 2-D-CSL0 algorithm for reconstructing an ISAR image is also simulated and analyzed. The values of the 2-D convolution kernel ***Ker*** used in the 2-D-CSL0 algorithm are shown in Fig. 8. For comparison, the result based on the chirp signal with a bandwidth of about 17.71 GHz and the RD algorithm is first shown in Fig. 9(a). Sparse imaging was then performed using an SSFC signal containing eight subpulses with a bandwidth of 0.5 GHz, which is also randomly distributed in the 17.71-GHz range. In addition, 50% of all bursts are randomly extracted in the azimuthal direction, i.e., the azimuthal undersampling rate is 50%. The reconstructed image obtained based on the 2-D-CSL0 algorithm is shown in Fig. 9(b), which is consistent with Fig. 9(a), indicating the validity of the 2-D-CSL0 algorithm for reconstructing the 2-D radar image. Fig. 10 shows the PSNR transit diagrams to investigate the effect of azimuthal undersampling ratio and subpulse bandwidth on the reconstruction performance. As can be seen, the phase transit boundary obtained based on the 2-D-CSL0 algorithm is closer to the upper left. This means that the proposed algorithm can achieve high-fidelity image reconstruction under lower azimuthal undersampling ratios and subpulse bandwidths compared to other algorithms. A comparison of the reconstruction performance of different algorithms at different SNRs is also given in Fig. 11. When the SNR is higher than 10 dB, the PSNR obtained based on the CSL0 algorithm is significantly higher than other algorithms. Thus, the proposed algorithm can significantly improve the

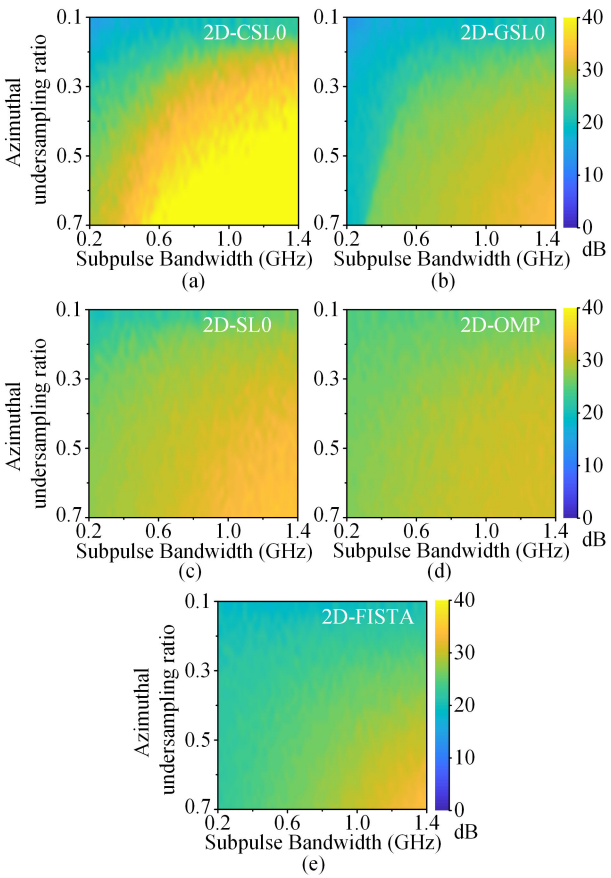

Fig. 10. PSNRs at different azimuthal undersampling ratios and subpulse bandwidths based on different algorithms. (a) 2-D-CSL0. (b) 2-D-GSL0. (c) 2-D-SL0. (d) 2-D-OMP. (e) 2-D-FISTA.

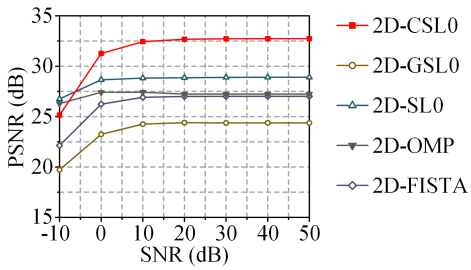

Fig. 11. PSNRs at different SNRs.

fidelity of recovered radar images under constrained resources such as frequency and aperture.

IV. Experiments and Results

A. Experimental Setup

An experimental system is built based on Fig. 1 to verify the performance of the proposed radar. In the transmitter, two arbitrary waveform generators (AWG, Keysight M8195A, and Tektronix AWG70000) are used to generate the reference and driving signals. The frequency of the reference signal fluctuates randomly, as shown in Fig. 12. The driving signal is a narrowband microwave chirp signal with a bandwidth of 500 MHz, a pulsewidth of 4 μs, and a period of 100 μs, and its time–frequency diagram and spectrum are shown

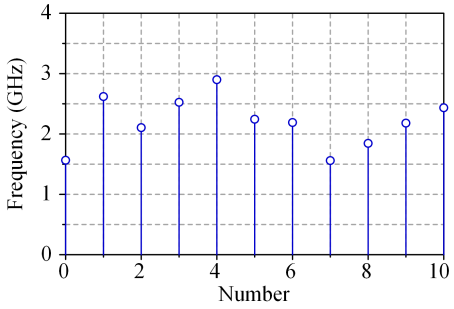

Fig. 12. Frequency of the reference signal.

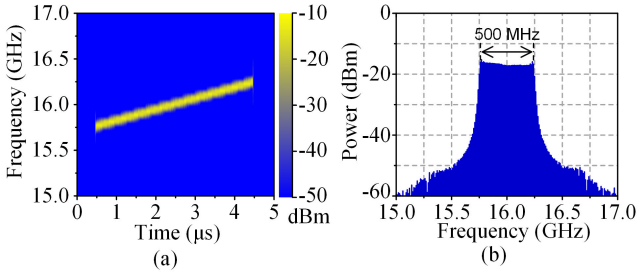

Fig. 13. (a) Time–frequency diagram. (b) Spectrum of the driving chirp signal.

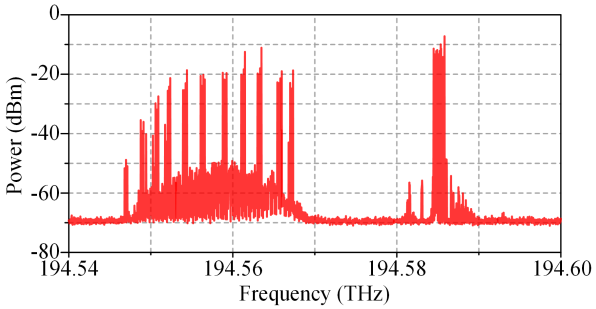

Fig. 14. Optical spectrum of the MWP-FC loop output.

in Fig. 13. In practice, the two signals can also be conveniently generated by other simple electronic signal generators since they are relatively narrowband. The microwave chirp signal is continuously upconverted in the MWP-FC loop. Its output optical spectrum is shown in Fig. 14. More than eight sidebands are excited on the left due to the continuous frequency conversion. A microwave signal with randomly stepped frequencies, namely, a random SSFC signal, is then generated and continuously transmitted by the transmitting antenna. The time–frequency diagram and spectrum of the random SSFC signal are shown in Fig. 15. As can be seen, more than eight subpulses covering a frequency range of >16 GHz are generated. The frequency intervals among the subpulses within the SSFC signal are diverse and can be adjusted by modifying the reference signal.

In the receiver, the radar echo is amplified and fed into a DOMZM (Eospace, AX-1 × 2–0MVS) working at the quadrature bias point. A 150-MHz BPD (Thorlabs, PDB450C-AC) follows the DOMZM for producing low-frequency dechirped signals. Finally, the sparse processing algorithm described in Section III is used to process the signal.

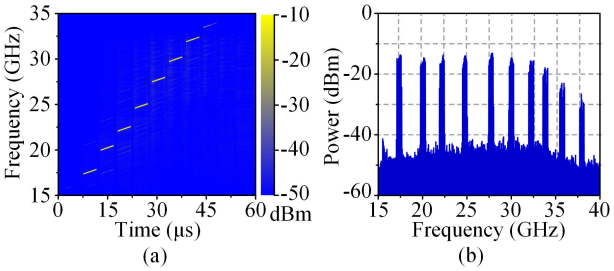

Fig. 15. (a) Time–frequency diagram. (b) Spectrum of the random SSFC signal.

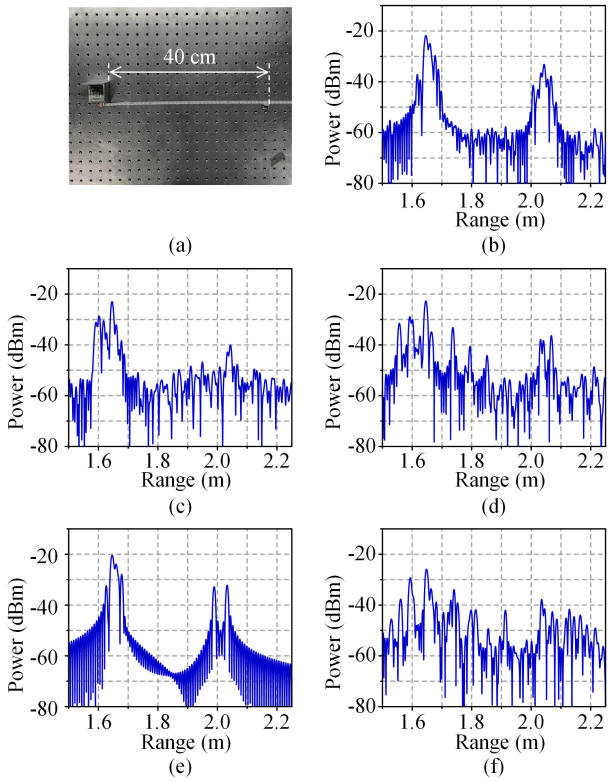

Fig. 16. (a) Photograph of the targets. Range images based on (b) CSL0, (c) GSL0, (d) SL0, (e) OMP, and (f) FISTA algorithms.

B. Sparse Range Imaging

First, two reflectors (size: 5.2 × 5.2 cm and 1.3 × 1.3 cm) at a distance of 40 cm are placed on an experimental platform as targets, as shown in Fig. 16(a). The dechirped signal of the targets is captured and processed using the proposed CSL0 algorithm. In this scenario, the SNR of the dechirped signal is approximately 16 dB. The duration of the reconstructed dechirped signal is about 141.7 μs, which corresponds to a chirp signal with a full bandwidth of about 17.71 GHz. Performing a Fourier transform on the reconstructed dechirped signal yields the range image shown in Fig. 16(b). The two peaks of the targets in Fig. 16(b) are located at 1.646 and 2.044 m. The difference between the two peaks is about 39.8 cm, close to the actual value of 40 cm. Different range images based on algorithms GSL0, SL0, OMP, and FISTA are shown in Fig. 16(c)–(f) for comparison with the proposed method. The range images based on the SL0 algorithm and

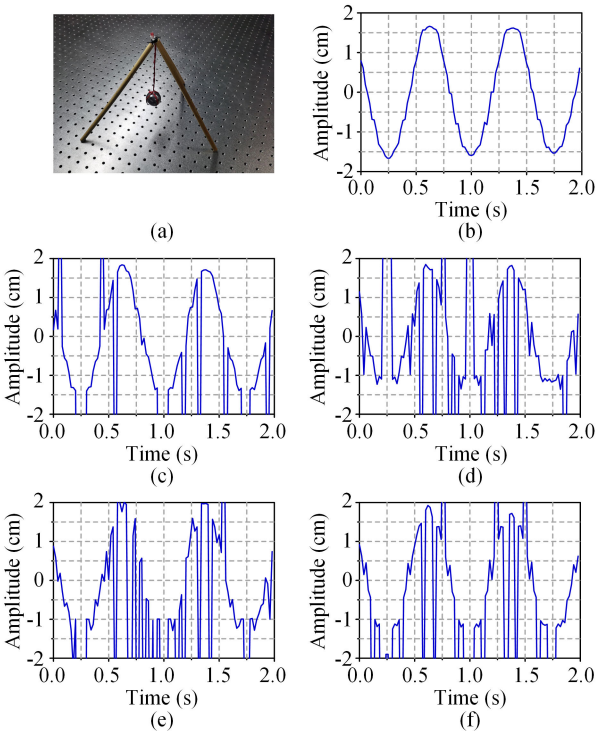

Fig. 17. (a) Photograph of the single pendulum. Motion trajectories obtained based on (b) CSL0, (c) GSL0, (d) SL0, (e) OMP, and (f) FISTA algorithms.

the FISTA algorithm have many strong clutters and do not correctly reconstruct the range image of the target. The range image based on the OMP algorithm has fewer clutters but fails to detect the weak target. The GSL0 algorithm is better than the other three algorithms but not as well as the proposed algorithm. Above all, the proposed algorithm improves the image contrast because of the convolution enhancement.

To further validate the advantages of the proposed system, a single pendulum with sinusoidal vibration is set up, as shown in Fig. 17(a). The single pendulum consists of a wire with a length of 12.5 cm and a ball with a diameter of 3.45 cm. Hence, its theoretical vibration frequency is about 1.321 Hz. In this experiment, the SNR of the obtained dechirped signal is approximately 15 dB. First, the range image is reconstructed using the proposed algorithm. The motion trajectory of the pendulum is extracted by tracking the peak position. The result is shown in Fig. 17(b), which shows a sinusoidal trajectory. By performing a Fourier transform on the trajectory, the vibrational frequency of a single pendulum is calculated to be approximately 1.325 Hz, which is very close to the theoretical frequency. The trajectories are also extracted based on the GSL0, SL0, OMP, and FISTA algorithms. The results are shown in Fig. 17(c)–(f). All of these traditional methods failed to extract the trajectory. This experimental result shows that the proposed method has unparalleled robustness.

At the end of this section, we investigate the highest range resolution that the proposed system can achieve. The radar signal generated in the transmitter is delivered to the receiver via two parallel microwave delay lines with a delay difference of 55 ps to emulate two scattered points with

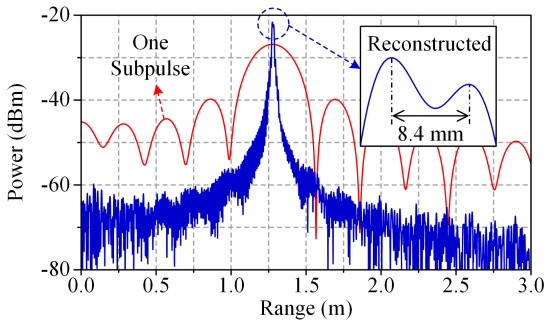

Fig. 18. Results based on one dechirped subpulse and the reconstructed dechirped signal.

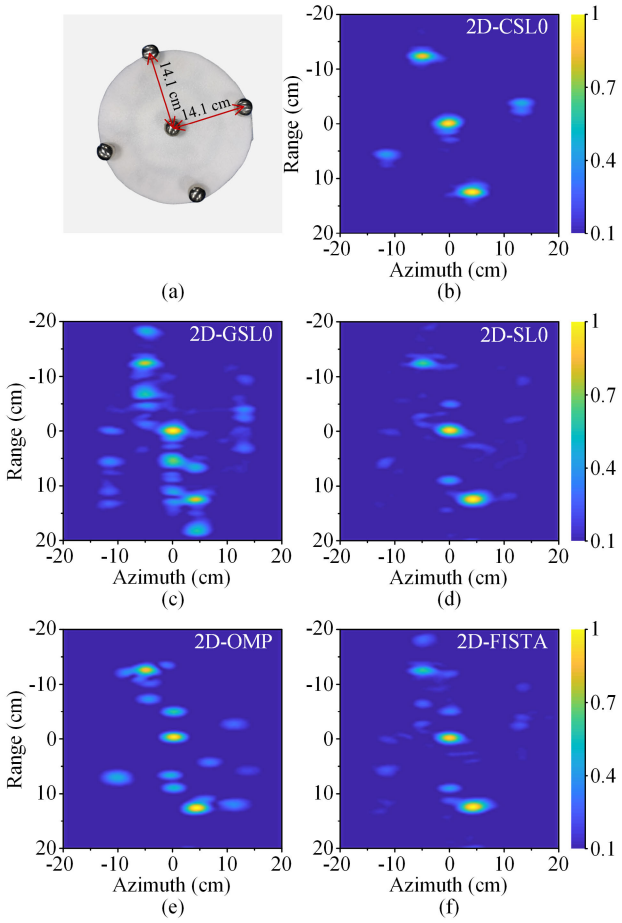

Fig. 19. (a) Photograph of the five balls. ISAR images of the five balls obtained based on (b) 2-D-CSL0, (c) 2-D-GSL0, (d) 2-D-SL0, (e) 2-D-OMP, and (f) 2-D-FISTA algorithms.

a distance difference of 8.3 mm. At this time, the SNR of the dechirped signal is approximately 24 dB. The range image reconstructed based on the proposed method is shown by the blue curve in Fig. 18. Two peaks can be clearly seen in positions 1.2752 and 1.2836 m. The measured distance difference is 8.4 mm, which is close to the set value. Using only one dechirped subpulse, i.e., using the same bandwidth as the driving signal, we obtain the range image shown by the red curve in Fig. 18. It can be seen that there is only one peak, meaning that two targets cannot be distinguished.

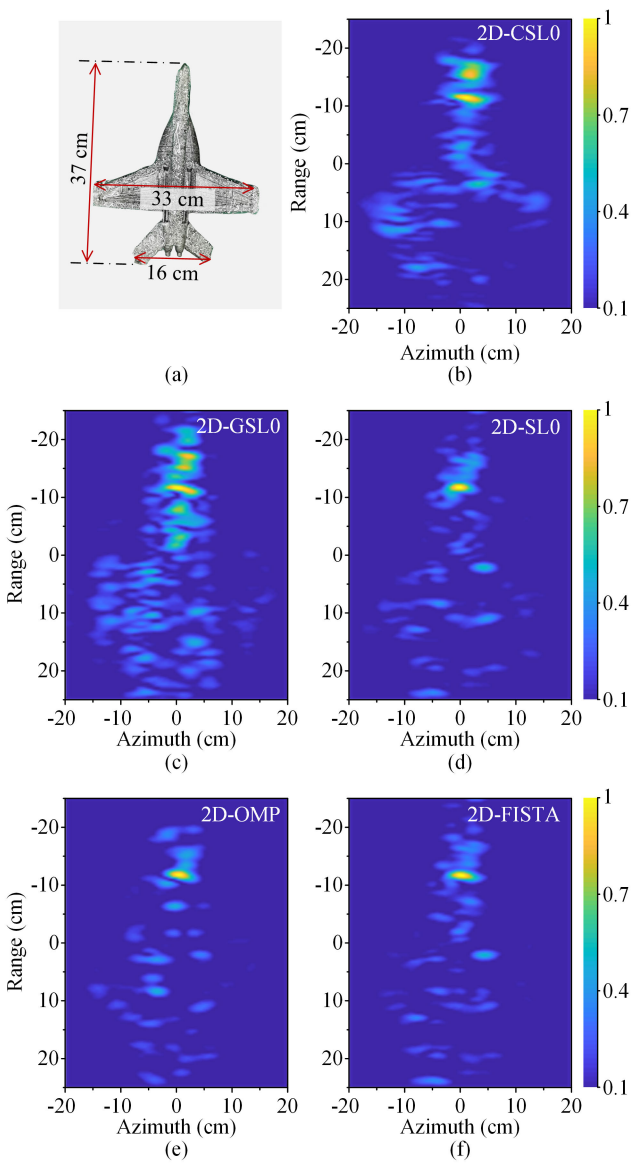

Fig. 20. (a) Photograph of the airplane model. ISAR images of the airplane model obtained based on (b) 2-D-CSL0, (c) 2-D-GSL0, (d) 2-D-SL0, (e) 2-D-OMP, and (f) 2-D-FISTA algorithms.

C. Sparse ISAR Imaging

We also construct an ISAR to verify the feasibility of the proposed method. To simplify the experiment, we placed the target on a rotating platform with a rotational speed of 4π/s. The target was observed continuously for 34.7 ms. During that time, the target was rotated by about 25°. In an observation period, 347 bursts can be provided, but we only use 18 bursts randomly to reduce the amount of data processed. First, five metal balls spaced 10 cm apart are placed on the rotating platform, as shown in Fig. 19(a). The observed dechirped signals attain an SNR of approximately 20 dB and are processed based on the proposed algorithm in Section III. A clear image is obtained, as shown in Fig. 19(b). The dechirped signals are also compared using algorithms such as 2-D-GSL0, 2-D-SL0, 2-D-OMP, and 2-D-FISTA, obtaining the images shown in Fig. 19(c)–(f), respectively. The images obtained by these traditional algorithms have more false targets than the proposed methods.

To further verify the validity of the proposed method, we replace the target with a complex aircraft model, as shown in Fig. 20(a). During this experiment, the SNR of the obtained dechirped signal is approximately 23 dB. Again, we reconstruct the radar image of the target by using different algorithms. The results are shown in Fig. 20(b)–(f). Only Fig. 20(b), i.e., the image obtained based on the 2-D-CSL0 algorithm, shows the outline of the aircraft model more clearly. The 2-D-GSL0 algorithm resulted in many false scatters, while the 2-D-SL0, 2-D-OMP, and 2-D-FISTA algorithms do not reconstruct enough scatters.

V. Discussion and Conclusion

In the experiments, we demonstrated the ability of the system to generate and process random SSFC signals. In practice, with the aid of microwave photonic frequency measurement for sensing the electromagnetic environment [23], the frequency intervals of the subpulses within the SSFC signal could be customized. Consequently, the presented methodology exhibits enhanced flexibility and practicality in comparison with prior works. It is important to mention that the center frequencies of the subpulses within the generated radar signals are arranged incrementally, which may potentially limit the practical implementation of the system in highly complex electromagnetic environments. Thus, it is essential to conduct further research on methods that enable the arbitrary tuning of the center frequency, thereby facilitating the generation of arbitrarily distributed spectra.

In addition, the system in this article is implemented based on discrete components. It can be deployed on various large-scale spatial platforms such as ground-based and airborne ones. Its deployment might be circumscribed within limited spaces, such as autonomous aerial vehicles, and satellites. Fortunately, the discrete components used in the system, such as lasers, modulators, and amplifiers, can be integrated to realize further improvement by developing the integrated photonics technology [45], [46], [47]. Subsequently, it becomes feasible to deploy the system on space-constrained platforms, such as autonomous aerial vehicles and satellites.

In conclusion, we have presented and demonstrated a microwave photonic radar for high-resolution sparse imaging. The radar enables the generating and processing of wideband random SSFC signals based on recirculating MWP-FC and a dechirping receiver. In addition, a CSL0 algorithm is proposed to improve the robustness of sparse imaging. In the experiment, a microwave photonic radar with a frequency range of >16 GHz, but the effective spectrum occupies only 4 GHz, is set up to achieve high-resolution sparse imaging at a subcentimeter level. The proposed method would greatly improve the anti-interception capability of the wideband radar, showing outstanding advantages in microwave imaging and recognition in complex environments.

References

[1] X. Chen, Z. Dong, Z. Zhang, C. W. Tu, T. Yi, and Z. He, "Very high resolution synthetic aperture radar systems and imaging: A review," *IEEE J. Sel. Topics Appl. Earth Observ. Remote Sens.*, vol. 17, pp. 7104–7123, 2024.

[2] W. L. Melvin and J. A. Scheer, *Principles of Modern Radar: Advanced Techniques*. Rijeka, Croatia: SciTech, 2012.

[3] J. Yao and J. Capmany, "Microwave photonics," *Sci. China Inf. Sci.*, vol. 65, no. 12, pp. 1–64, Dec. 2022.

[4] S. Pan and Y. Zhang, "Microwave photonic radars," *J. Lightw. Technol.*, vol. 38, no. 19, pp. 5450–5484, Oct. 1, 2020.

[5] S. Pan, X. Ye, Y. Zhang, and F. Zhang, "Microwave photonic array radars," *IEEE J. Microw.*, vol. 1, no. 1, pp. 176–190, Jan. 2021.

[6] P. Ghelfi et al., "A fully photonics-based coherent radar system," *Nature*, vol. 507, no. 7492, pp. 341–345, Mar. 2014.

[7] Z. Yang, L. Zhang, H. Zhang, H. Yang, Z. Lyu, and X. Yu, "Photonic THz InISAR for 3D positioning with high resolution," *J. Lightw. Technol.*, vol. 41, no. 10, pp. 2999–3006, May 15, 2023.

[8] Q. Guo, S. Liu, T. Chai, H. Chen, K. Yin, and C. Ji, "Real-time photonic radar with multi-band agility based on mode locked laser," *IEEE Photon. Technol. Lett.*, vol. 36, no. 2, pp. 71–74, Jan. 2024.

[9] F. Zhang et al., "Photonics-based broadband radar for high-resolution and real-time inverse synthetic aperture imaging," *Opt. Exp.*, vol. 25, no. 14, pp. 16274–16281, Jul. 2017.

[10] R. Li et al., "Demonstration of a microwave photonic synthetic aperture radar based on photonic-assisted signal generation and stretch processing," *Opt. Exp.*, vol. 25, no. 13, pp. 14334–14340, Jun. 2017.

[11] A. Wang et al., "Ka-band microwave photonic ultra-wideband imaging radar for capturing quantitative target information," *Opt. Exp.*, vol. 26, no. 16, pp. 20708–20717, Aug. 2018.

[12] J. Cao et al., "Photonic deramp receiver for dual-band LFM-CW radar," *J. Lightw. Technol.*, vol. 37, no. 10, pp. 2403–2408, May 15, 2019.

[13] Z. Mo et al., "Microwave photonic de-chirp receiver for breaking the detection range swath limitation," *Opt. Exp.*, vol. 29, no. 7, p. 11314, Mar. 2021.

[14] R. Li et al., "PFDIR—A wideband photonic-assisted SAR system," *IEEE Trans. Aerosp. Electron. Syst.*, vol. 59, no. 4, pp. 4333–4346, Aug. 2023.

[15] Z. Huang, J. Wo, C. Li, Q. Chen, and J. Yao, "Dual-functional microwave photonic system for target detection and frequency measurement," *IEEE Trans. Microw. Theory Techn.*, vol. 72, no. 11, pp. 6648–6656, Nov. 2024.

[16] S. Peng et al., "High-resolution W-band ISAR imaging system utilizing a logic-operation-based photonic digital-to-analog converter," *Opt. Exp.*, vol. 26, no. 2, p. 1978, Jan. 2018.

[17] P. Zhou, R. Zhang, N. Li, Z. Jiang, and S. Pan, "An RF-source-free reconfigurable microwave photonic radar with high-resolution and fast detection capability," *J. Lightw. Technol.*, vol. 40, no. 9, pp. 2862–2869, May 1, 2022.

[18] G. Sun, Y. Zhou, Y. He, X. Yu, F. Zhang, and S. Pan, "Photonics-based MIMO radar with broadband digital coincidence imaging," *IEEE Trans. Microw. Theory Techn.*, vol. 72, no. 12, pp. 6996–7003, Jun. 2024.

[19] X. Zhang, H. Zeng, J. Yang, Z. Yin, Q. Sun, and W. Li, "Novel RF-source-free reconfigurable microwave photonic radar," *Opt. Exp.*, vol. 28, no. 9, p. 13650, Apr. 2020.

[20] C. Ma et al., "Microwave photonic imaging radar with a sub-centimeter-level resolution," *J. Lightw. Technol.*, vol. 38, no. 18, pp. 4948–4954, Sep. 2020.

[21] Y. Liu, Z. Zhang, M. Burla, and B. J. Eggleton, "11-GHz-bandwidth photonic radar using MHz electronics," *Laser Photon. Rev.*, vol. 16, no. 4, pp. 1–11, Feb. 2022.

[22] C. Ma et al., "Distributed microwave photonic MIMO radar with accurate target position estimation," *IEEE Trans. Microw. Theory Techn.*, vol. 71, no. 4, pp. 1711–1719, Apr. 2023.

[23] D. Zhu et al., "Microwave photonic cognitive radar with a subcentimeter resolution," *IEEE Trans. Microw. Theory Techn.*, vol. 72, no. 9, pp. 5519–5529, Sep. 2024.

[24] J. Wei, D. Kwon, S. Zhang, S. Pan, and J. Kim, "All-fiber-photonics-based ultralow-noise agile frequency synthesizer for X-band radars," *Photon. Res.*, vol. 6, no. 1, pp. 12–17, Jan. 2018.

[25] B. Zhao et al., "Shallow-layers-detection ice sounding radar for mapping of polar ice sheets," *IEEE Trans. Geosci. Remote Sens.*, vol. 60, 2022, Art. no. 4301010.

[26] P. Zhou, F. Zhang, X. Ye, Q. Guo, and S. Pan, "Flexible frequency-hopping microwave generation by dynamic control of optically injected semiconductor laser," *IEEE Photon. J.*, vol. 8, no. 6, pp. 1–9, Dec. 2016.

[27] T. Hao, H. Ding, W. Li, N. Zhu, Y. Dai, and M. Li, "Dissipative microwave photonic solitons in spontaneous frequency-hopping opto-electronic oscillators," *Photon. Res.*, vol. 10, no. 5, p. 1280, May 2022.

[28] Z. Zhang, Y. Liu, and B. J. Eggleton, "Photonic generation of 30 GHz bandwidth stepped-frequency signals for radar applications," *J. Lightw. Technol.*, vol. 40, no. 14, pp. 4521–4527, Jul. 15, 2022.

[29] C. Ma et al., "High-resolution microwave photonic radar with sparse stepped frequency chirp signals," *IEEE Trans. Geosci. Remote Sens.*, vol. 60, 2022, Art. no. 2007010.
[30] C. Ma, X. Wang, Y. Yang, Z. Ding, and S. Pan, "Coherent stepped-frequency waveform generation based on recirculating microwave photonic frequency conversion," *Opt. Lett.*, vol. 48, no. 19, p. 4985, Oct. 2023.
[31] V. C. Chen and M. Martorella, *Inverse Synthetic Aperture Radar Imaging: Principles, Algorithms and Applications*. Hertfordshire, U.K.: SciTech, 2014.
[32] J. Yang, Y. Wang, and Y. Ma, "Novel approach for sparse aperture inverse synthetic aperture radar imaging via improved alternating direction method of multipliers algorithm," *IET Radar, Sonar Navigat.*, vol. 17, no. 10, pp. 1581–1597, Oct. 2023.
[33] R. Baraniuk and P. Steeghs, "Compressive radar imaging," in *Proc. IEEE Radar Conf.*, Waltham, MA, USA, Apr. 2007, pp. 128–133.
[34] L. C. Potter, E. Ertin, J. T. Parker, and M. Cetin, "Sparsity and compressed sensing in radar imaging," *Proc. IEEE*, vol. 98, no. 6, pp. 1006–1020, Jun. 2010.
[35] E. Giusti, D. Cataldo, A. Bacci, S. Tomei, and M. Martorella, "ISAR image resolution enhancement: Compressive sensing versus state-of-the-art super-resolution techniques," *IEEE Trans. Aerosp. Electron. Syst.*, vol. 54, no. 4, pp. 1983–1997, Aug. 2018.
[36] J. Tropp and A. C. Gilbert, "Signal recovery from partial information via orthogonal matching pursuit," *IEEE Trans. Inf. Theory*, vol. 53, no. 12, pp. 4655–4666, Dec. 2007.
[37] A. Beck and M. Teboulle, "A fast iterative shrinkage-thresholding algorithm for linear inverse problems," *SIAM J. Imag. Sci.*, vol. 2, no. 1, pp. 183–202, Jan. 2009.
[38] H. Mohimani, M. Babaie-Zadeh, and C. Jutten, "A fast approach for overcomplete sparse decomposition based on smoothed ℓ_0 norm," *IEEE Trans. Signal Process.*, vol. 57, no. 1, pp. 289–301, Jan. 2009.
[39] Z. Liu, X. Wei, and X. Li, "Decoupled ISAR imaging using RSFW based on twice compressed sensing," *IEEE Trans. Aerosp. Electron. Syst.*, vol. 50, no. 4, pp. 3195–3211, Oct. 2014.
[40] J. Fang, Z. Xu, B. Zhang, W. Hong, and Y. Wu, "Fast compressed sensing SAR imaging based on approximated observation," *IEEE J. Sel. Topics Appl. Earth Observ. Remote Sens.*, vol. 7, no. 1, pp. 352–363, Jan. 2014.
[41] Y. Fang, J. Wu, and B. Huang, "2D sparse signal recovery via 2D orthogonal matching pursuit," *Sci. China Inf. Sci.*, vol. 55, pp. 889–897, Mar. 2012.
[42] S. Li, G. Zhao, W. Zhang, Q. Qiu, and H. Sun, "ISAR imaging by two-dimensional convex optimization-based compressive sensing," *IEEE Sensors J.*, vol. 16, no. 19, pp. 7088–7093, Oct. 2016.
[43] A. Ghaffari, M. Babaie-Zadeh, and C. Jutten, "Sparse decomposition of two dimensional signals," in *Proc. IEEE Int. Conf. Acoust., Speech Signal Process.*, Taipei, China, Apr. 2009, pp. 3157–3160.
[44] S. H. Ghalehjegh et al., "Fast block-sparse decomposition based on SL0," in *Proc. LVA/ICA*, Saint Malo, France, Jan. 2010, pp. 426–433.
[45] S. Li et al., "Chip-based microwave-photonic radar for high-resolution imaging," *Laser Photon. Rev.*, vol. 14, no. 10, pp. 1–6, Aug. 2020.
[46] S. Zhu et al., "Integrated photonic millimeter-wave radar based on thin-film lithium niobate," in *Proc. CLEO*, Charlotte, NC, USA, May 2024, pp. 1–2.
[47] W. Ma, R. Wang, J. Liu, and W. Li, "High-performance integrated microwave photonic transceiver for dual-band synthetic aperture radar," *J. Lightw. Technol.*, vol. 42, no. 21, pp. 7482–7490, Nov. 15, 2024.